Flow (2023), **x** E1
doi:10.1017/flo.2023.xx

FLOW CAMBRIDGE UNIVERSITY PRESS

RESEARCH ARTICLE

Impact of Large-Scale Freestream Turbulence on a Pitching Airfoil

ThankGod Enatimi Boye, Kamal Djidjeli and Zheng-Tong Xie*[1,1]

[1]Faculty of Engineering and Physical Sciences, University of Southampton, SO17 1BJ, United Kingdom.
*Corresponding author. E-mail: z.xie@soton.ac.uk

Received: XX 2023; **Revised:** XX XX 2023; **Accepted:** XX XX 2023

Keywords: Dynamic stall; Large-eddy simulation; Integral length-scale; Dispersive shear stress; Pitching blade wake

Abstract

This paper investigates the impact of large-scale turbulence on the aerodynamic characteristics of a pitching wind turbine blade at Reynolds number 135,000, of which the cross section is NACA0012 airfoil with a constant chord length. Large-eddy simulations (LES) at reduced frequencies, k_{red} = 0.05 and 0.1 were validated against reference data in the literature. An efficient method capable of generating synthetic large-scale turbulence at the inlet was applied by using two streamwise integral length-scales $L_x = 1c$ and $1.5c$, which represent energetic turbulent eddies at the height where wind turbine operates. For $k_{red} = 0.1$, the change in the maximum lift coefficient at the dynamic stall angle near the maximum angle of attack is by an average of 20% decrease, and during the downstroke it is by an average of 22% decrease, compared to the smooth inflow. A higher reduced frequency ($k_{red} = 0.2$) does not further evidently change the lift, drag and moment coefficients, and the inflow-turbulence disordered lead-edge vortices. The turbulent shear stress and the phase-averaged dispersive shear stress in the wake are in the same magnitude but with respectively negative and positive signs, suggesting that the large-scale phase-averaged fluctuations transfer momentum in an opposite direction compared to the turbulent fluctuations, reduced the resistance to the suction side flow, and subsequently enhanced the averaged lift coefficient. This demonstrates the crucial importance of the large-scale non-turbulence unsteadiness in the wake of a pitching wing.

Impact Statement This paper investigates the impact of large-scale turbulence on the aerodynamic characteristics of a pitching wind turbine blade at Reynolds number 135,000, of which the cross section is NACA0012 airfoil with a constant chord length. Large-eddy simulations at reduced frequencies, k_{red} = 0.05 and 0.1 were validated. An efficient method capable of generating synthetic large-scale turbulence at the inlet was applied by using two streamwise integral length-scales $L_x = 1c$ and $1.5c$. For $k_{red} = 0.1$, the change in the maximum lift coefficient at the dynamic stall angle near the maximum angle of attack is evident. A higher reduced frequency ($k_{red} = 0.2$) does not further evidently change the lift, drag and moment coefficients. The turbulent shear stress and the phase-averaged dispersive shear stress in the wake are in the same magnitude but with respectively negative and positive signs, suggesting that the large-scale phase-averaged fluctuations transfer momentum in an opposite direction compared to the turbulent fluctuations, reduced the resistance to the suction side flow, and subsequently enhanced the averaged lift coefficient. This study demonstrates the crucial importance of the large-scale non-turbulence unsteadiness in the wake of a pitching wing.
Although the present research has a focus on the aerodynamics of wind turbine blades, it can also be applicable for the relevant topics in aeronautics, acoustics and other wind engineering areas.

1. Introduction

In the recent years, the interaction of free-stream turbulence and static or unsteady wing has attracted a greater attention of researchers in aeronautics (e.g. Chiereghin et al., 2017; Badoe et al., 2019; Zhang et al., 2023), acoustics (e.g. Lau et al., 2013; Bowen et al., 2023), and wind engineering (e.g. Kim and Xie, 2016; Huang et al., 2020; Boye, 2022) areas. The meteorological variations of wind direction can generate large-scales unsteadiness. Wind gusts, which are common unsteady phenomena, may damage or completely destroy the wind turbine blades (Shohag et al., 2017; Hand, 2004). The need to reduce the cost of energy that wind turbine produces facilitates the design of modern wind turbines with rotor disc diameter greater than 100 m and hub height over 200 m above the ground level. At this height, wind turbines are more exposed to high wind speed and large-scale atmospheric boundary layer (ABL) turbulence (Stull, 1988). Turbulent eddies in the ABL are usually much greater than the wind turbine-blade chord length (Kaimal and Finnigan, 1994). The turbulent eddy size in the ABL ranges from 0.001 m to 500 m. The turbulent integral length scales greater than the chord length are considered "large scale".

1.1. Dynamic stall in large-scale turbulence

The dynamic stall under the influence of large-scale incoming turbulence has not been studied rigorously, and is not fully understood. For static airfoils, considerable experimental and numerical studies for the effects of freestream turbulence on the aerodynamic characteristics have been reported in the literature. However, there are a very small number of experimental studies of the effect of freestream turbulence on a pitching airfoil/blade, and even fewer numerical studies(Gandhi et al., 2017). This could be due to technical difficulties in measuring the surface pressure accurately during the dynamic stall process for an experimental study - particularly for high reduced frequency (Lee and Gerontakos, 2004). Numerical simulation (e.g., large eddy simulation (LES)) would involve high computational costs but would not suffer from such technical difficulties(Huang et al., 2020; Boye and Xie, 2022).

The studies (Amandolèse and Széchényi, 2004; Kim and Xie, 2016; Huang et al., 2020) of freestream turbulence effects on the dynamic stall of a pitching airfoil focus on turbulent intensity and small integral length scale, e.g. $L_x \leq 0.3c$, where c is the chord length. They infer that an increase of the turbulent intensity increased the lift coefficient, particularly during the downstroke of the airfoil motion. On the other hand, research on the effect of large-scale freestream turbulence on the dynamic stall of a pitching turbine blade is scarce in the literature. Table 1 shows a summary of studies which have attempted to investigate the effect of freestream turbulence on the dynamic stall of a pitching airfoil. The majority of those studies focused on the effects of turbulence intensity and small-scale turbulence.

1.2. Why study large-scale freestream turbulence?

Stack (1931) stated that the effect of the large-scale freestream turbulence on the aerodynamics characteristics of airfoil/blade is of greater importance than that of the turbulence intensity changes. It is not surprising that only trivial efforts were given to unravel postulation. One reason is that it is relatively easy to generate freestream turbulence with different turbulent intensity and with small integral length scales that are much smaller than the chord length of the airfoil/blade in an experiments (Ravi et al., 2012). These are also well within the supercomputer's capability when using a numerical approach (Kim and Xie, 2016; Huang et al., 2020). On the contrary, a study on large-scale freestream turbulence (e.g. with the integral length scales greater than the chord length of an airfoil) challenges wind tunnel experiments and numerical simulations. Therefore, a salient question arises- what large integral length scale would be the priority to study to bridge the knowledge gap (i.e., lack of understanding of large-scale turbulence effect) within our current numerical and experimental capability?

Wind tunnel measurements (Maldonado et al., 2015; Ravi et al., 2012, 2013) suggested that large-scales eddies comparable in size to the chord length significantly improves the aerodynamic performance

Table 1: Summary of literature on the effect of turbulence on dynamic stall of an pitching airfoil, $\boldsymbol{\alpha_0}$ and $\boldsymbol{\alpha_1}$ are mean angle of attack and pitching amplitude respectively, **AR** aspect ratio, $\boldsymbol{L_x}$ integral length-scale and $\boldsymbol{TI}$ turbulent intensity. wT^* denotes the wake turbulence from a small static cylinder placed approximately one chord length upstream of the aerofoil.

Authors	Method	k_{red}	$Re[10^6]$	$TI[\%]$	c [m]	L_x/c	$AR[z/c]$	Airfoils	$\alpha_0[^\circ]$	$\alpha_1[^\circ]$
Amandolese et al. (2004)	Exp.	0.0183 - 0.183	≈ 1	1.1 - 7.5	0.5	0.24	3.2	NACA 63_4 - 421	8 - 20	2 - 8
Wang et al. (2012)	DES	0.10	0.135	0.08	0.15	0.4	0.375	NACA 0012	10	15
Kim and Xie (2016)	LES	0.025 - 0.1	0.135	5 - 10	1	0.3	0.5	NACA 0012	10	15
Yu et al. (2017)	Exp.	0.09 - 0.27	0.0045	0.5 - 6.9	0.01	0.03	0.3	NACA 0015	0	30
Gandhi et al. (2017)	DNS	0.16, 0.25	0.044	wT^*	1	wT^*	-	NACA 0012	15	10
Algozino et al. (2018)	Exp.	0.005 - 0.025	0.023 -0.053	0.5 - 1	0.1	0.5	0.4	Flat-plate	0.2	0 - 45
Huang et al. (2020)	LES	0.2	0.15	5	1	0.15	1	NACA 0012	15	10

of static airfiols, which opposes the concluding remark drawn in wind tunnel experiments (Mahmoodi-lari, 2012; Herbst et al., 2018) and LES studies (Wang and Xiao, 2021). The lack of a consensus view of large-scale turbulence effect on the aerodynamics performance of static airfoil urges further studies on large-scale freestream turbulence. As a start, this study investigated the impact of large-scale freestream turbulence on the aerodynamic characteristics of pitching wind turbine blades, also aiming to shedding some light on studies of static blades.

1.3. Wake dispersive stress

Studies of the wind turbine wake dynamics and characterisation, and wake turbulence dissipation are reported in the literature (e.g. Raverdy et al., 2003; Aitken et al., 2014; Jimenez et al., 2007; Sun et al., 2020; Lundquist and Bariteau, 2015; Browne et al., 1987). The study of the motion of wind turbine blade (e.g. periodic pitching motion) on the wake turbulence is crucial for the understanding of the aerodynamics of wind turbine blades.

The dispersive shear stress is widely used to quantify the global vertical momentum exchange (or shear stress) over a certain spatial size of urban or forest area, due to the variations of the local time-mean streamwise and vertical velocities because the heterogeneity of the underlying surface (e.g. Xie and Fuka, 2018). To assess the contribution of the periodic pitching motion of wind turbine blade to the turbulence shear stresses in the wake, the concept of the dispersive shear stresses is used. Or it can be denoted "phase shear stress", which is the component of the momentum flux due to the phase-averaged velocity fluctuations, where the phase-averaged velocity fluctuation is the difference between phase-averaged velocity and the total average of the time-mean velocity (Boye, 2022) (more details presented in section 4.4). It is calculated by averaging over the entire time duration the production of the phase-averaged streawise and cross-flow velocity.

1.4. Outline of the paper

This paper reports the impact of large integral length-scales, i.e. with the streamwise integral length equal or greater than the chord length, which are much greater than those reported in the literature. The NACA 0012 airfoil oscillating in pitching motion is placed in a freestream turbulent flow at a moderate Reynolds number Re = 1.35 x 10^5, based on the chord length and the freestream velocity. Section 2, includes the governing equations of LES, numerical settings and synthetic inflow turbulence generation settings. The mesh and domain sensitivity studies for large-scale turbulence simulations are presented in Section 2.3. Section 3 shows the validation for a test case with small-scale freestream turbulence. Section 4 presents the impact of large-scale freestream turbulence on pitching blade. Finally, Section 5 presents discussions and draws concluding remarks.

2. Methodology and settings

2.1. Governing equations

The applied governing equations are the unsteady filtered Navier-Stokes equations for an incompressibe flow. The set of equations are written below (Kim and Xie, 2016),

$$\frac{\partial \bar{u}_i}{\partial x_i} = 0 \tag{1}$$

$$\frac{\partial \bar{u}_i}{\partial t} + \frac{\partial \bar{u}_i \bar{u}_j}{\partial x_j} = -\frac{1}{\rho}\frac{\partial \bar{p}}{\partial x_i} + \frac{\partial}{\partial x_j}\left(\nu \frac{\partial \bar{u}_i}{\partial x_j} - \tau^r_{ij}\right), \tag{2}$$

where "$\bar{}$" denotes filtering operation, u_i is the filtered or resolved velocity component in the x_i direction, t is time, ρ is the air density, p is the static pressure, and ν is the kinematic viscosity. $\tau_{ij}^r = \overline{u_i u_j} - \bar{u}_i \bar{u}_j$ is the subgrid-scale (SGS) stress tensor, and is modelled following the Boussinesq assumption,

$$\tau_{ij}^r = -2\nu_t \bar{S}_{ij} + \frac{1}{3}\delta_{ij}\tau_{kk}, \tag{3}$$

where the Kronecker delta $\delta_{ij} = 1$ for $i = j$, otherwise $\delta_{ij} = 0$; ν_t is the SGS viscosity, and $\bar{S}_{ij}$ is the rate-of-strain tensor for the resolved scales defined by

$$\bar{S}_{ij} = \frac{1}{2}\left(\frac{\partial \bar{u}_i}{\partial x_j} + \frac{\partial \bar{u}_j}{\partial x_i}\right). \tag{4}$$

Here, the mixed time scale (MTS) SGS model (Inagaki et al., 2005) with improved model constant of $C_{MTS} = 0.03$ and $C_T = 10$ (Krishnan et al., 2009) was adopted.

2.2. Adopted numerical settings

Figure 1 illustrates the studied pitching airfoil motion at various phase angles. The NACA 0012 airfoil profile is used and the pitching pivot is located at quarter chord length from the leading edge. The pitching motion follows the function expressed in Equation 5,

$$\alpha(t) = \alpha_0 + \alpha_1 sin(\omega t) \tag{5}$$

where $\alpha_0 = 10°$ is the mean angle of attack, $\alpha_1 = 15°$ is the pitching amplitude, ω is the airfoil angular velocity, and t is the time of the airfoil pitching motion.

The reduced frequency (k_{red}), which is a principal non-dimensional parameter (Carr, 1985) for a pitching motion airfoil is expressed in Equation 6,

$$k_{\text{red}} = \frac{\pi f c}{U_\infty}, \tag{6}$$

where f is frequency, c is chord length and U_∞ is freestream velocity.

The Reynolds number, $Re = 1.35 \times 10^5$ based on the chord length c and freestream velocity U_∞, is used for the present study, which is within the range of Re number for small and medium-size wind turbines. Moreover, the Re number dependency is less for a pitching airfoil in a freestream turbulent flow than a static one in a smooth inflow. McCroskey (1982) reported that for a periodically pitching airfoil, the Reynolds number effect is small. Kasibhotla and Tafti (2015) compare the data at $Re = 10^5$ and 10^6, and state that the same physic processes are observed. Therefore, the data generated in the current study is beneficial for fundamental understanding, and can be used as reference data for the study of pitching wind turbine blade at much higher Reynolds numbers. The reduced frequencies k_{red} = 0.1 and 0.2 were employed in the study.

The airfoil pitching motion was enabled with the aid of dynamic mesh technique for the cells in the near-airfoil region, which accommodates the deformation of the domain due to the airfoil motion. This was achieved with the PimpleDyMFoam solver in OpenFOAM, which have the same algorithm characteristics as PIMPLE designed for static simulation. In the PimpleDyMFoam solver, the pre-defined sequence of the dynamic mesh, which accommodates the airfoil motion is controlled by re-calculation of relative nodal positions at each time step according to a pre-defined boundary motion and diffusivity, γ. Jasak and Tuković (2006) tested the influence of γ on mesh quality around a moving airfoil trailing-edge, and suggested that the quadratic diffusivity (Equation 7) enhanced the superiority of the mesh

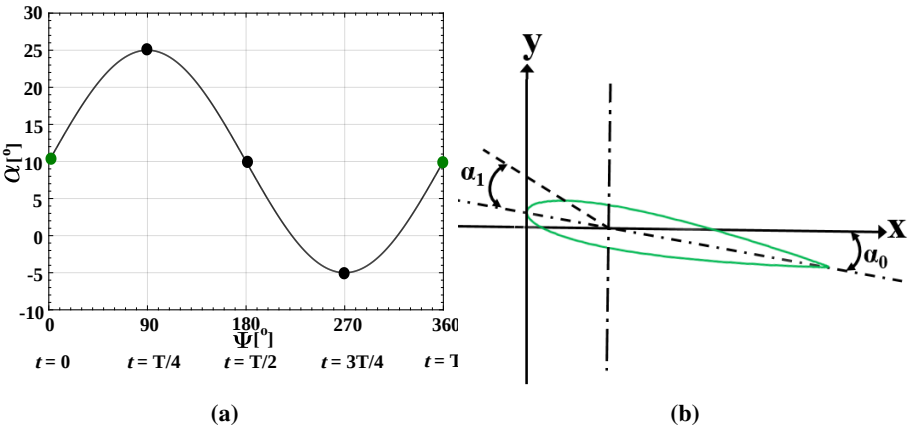

Fig. 1: A sketch of pitching airfoil motion and the coordinate system with the z coordinate in right hand rule. (a) the angle of attack (α) as a function of phase angle (Ψ), where t is the time, T is the period of the pitching cycle. (b) a pitching airfoil at neutral position with the pitching pivot located at quarter chord length from the leading edge (see Equation 5).

quality when compared to the constant, linear and exponential diffusivity,

$$\gamma = \frac{1}{l^2}, \text{(quadratic)}; \tag{7}$$

where l is the cell centre distance to the nearest selected boundary. The quadratic diffusivity was adopted in the current study.

The transient incompressible solver in OpenFOAM 2.3.0 was used throughout this work. Considering the robustness and efficiency the PIMPLE algorithm was employed for the pressure-velocity coupling (Greenshields, 2017), with two outer iterations, and three pressure correctors. A second-order implicit scheme was implemented for the temporal discretization, and the convective term uses the Gamma differencing scheme, a hybrid scheme developed by Jasak et al. (1999). The time step Δt was set to 9.5×10^{-4} s that satisfied the mean courant number $CFL \leq 1$ and the maximum $CFL \leq 3$ for all the cases simulated. The pitching periods for reduced frequencies $k_{\text{red}} = 0.1$ and 0.2, are respectively $T = 31.41$ s and 15.7 s resulting in a very small ratio $\Delta t/T$ ranging from 3.02×10^{-5} to 6.0×10^{-5}. The time step used in the current study is similar to the time-step used in (Boye and Xie, 2022). Initialisation duration was one cycle of oscillation, and the subsequent three cycles were used for the post-processing. These time durations for the simulations were respectively the same as those in Kim and Xie (2016); Huang et al. (2020).

2.3. Geometry and mesh generation

The mesh used for the validation for smooth flow was the original $3DM_3$ hybrid C-H type structured mesh, which was checked rigorously in terms of mesh sensitivity, and was used for large-eddy simulations in Boye and Xie (2022). The inlet of $3DM_3$ (Boye and Xie, 2022) was modified to form a new H-type structured mesh (see Fig. 2 and Table 2), for easy implementation of the synthetic inflow turbulence generation. It is to be noted that the resolution in the other regions, including the near-wall resolution, is kept the same in the modified $3DM_3$.

The boundaries BC1, BC2, and BC3 were set with inflow boundary conditions. The boundary BC4 was set with outflow boundary conditions. No-slip wall boundary conditions were set for the airfoil surface. Symmetric boundary conditions were set for the two lateral sides of the domain. Kim and Xie (2016) argued that simulations of pitching airfoil were much less sensitive to the lateral boundary

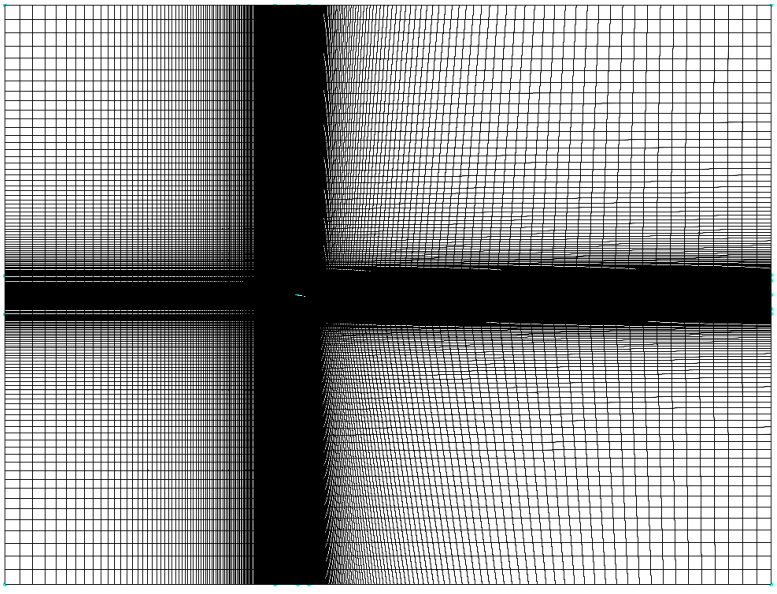

(a)

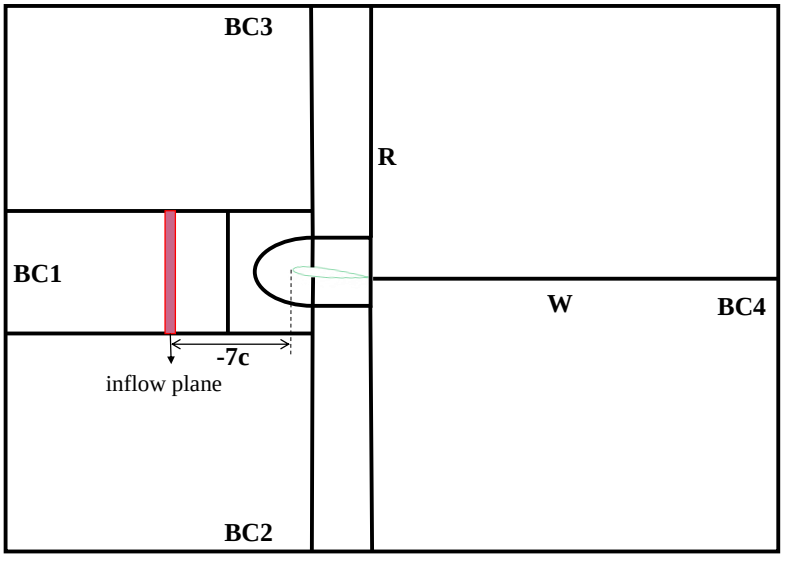

(b)

Fig. 2: (a) Modified 3DM$_3$ mesh topology – an H-type mesh. (b) A sketch of the modified computational domain (not to scale) (see the coordinate system in Fig. 1). BC1, BC2, and BC3 with inflow boundary conditions, BC4 with outlet boundary conditions, no-slip wall boundary conditions for the airfoil surface, symmetric boundary conditions for the two lateral sides of the domain. R is the half-width of the domain in the y direction, W is the wake length from the trailing edge to the outlet

Table 2: A summary of the computational domain size in unit c and number of grid points on the domain boundaries for 3DM$_3$ (see Fig. 2). R is the half-width of the domain in the y direction, and is the distance from BC1 to the trailing edge. W is the wake length from the trailing edge to the outlet. s is span length. N_{up} and N_{low} are number of points in the suction and pressure sides of airfoil respectively. N_z denotes the number of points in the spanwise direction.

R/c	W/c	s/c	N_R	N_W	N_{up}	N_{low}	N_z
20	33	3	234	125	367	193	120

conditions compared to those of a static one, because the flows were more dominant by the pitching motion. Furthermore, given that the final chosen span of the domain was three times chord length, the effect of the lateral boundary conditions on the core region of the domain were small (Boye and Xie, 2022). The span-length sensitivity study for large-scale freestream turbulence (Boye, 2022) (not show here), showed that a span-length s must be at least four times the spanwise integral length scale L_z. This is followed in the present study (Table 3).

2.4. Inflow turbulence generation for LES

A divergence-free synthetic inflow turbulence generation approach denoted XCDF (Kim et al., 2013), was applied, imposing correlations by using an exponential function to satisfy the prescribed integral length and time scales (Xie and Castro, 2008). It should be noted that one of the attractive features of synthetic inflow generation methods (Xie and Castro, 2008; Kim et al., 2013) is the use of the exponential correlations, which significantly reduces the computational cost compared to the early digital filter based approaches (e.g. see the review paper Wu, 2017), and generates a time-evolving three-dimensional turbulence field with power spectra consisting of a wide inertial subrange. This method is the combination of the digital filter method and the forward stepwise methods, and is also denoted Hybrid Forward Stepwise (HFS) approach.

The synthetic turbulence is generated at a 2D transverse plane at $x/c = -7$ (i.e. 7c upstream from the leading edge) shown in Fig. 2 (b) . The inflow plane placed at x/c = -7 is consistent with that in Kim and Xie (2016); Kim (2013) for a similar computational domain, which ensures adequate development of the synthetic turbulence before it reaches the region of interest.

3. Validation for small-scale freestream turbulence

3.1. Freestream turbulent parameters

Table 3 shows the turbulence parameters used in the current study. Freestream turbulence with the streamwise integral length-scale $L_x \geq 1c$ is categorised into "large scale" in this study, which is consistent with that in Sicot et al. (2006). It is to be noted that the"large-scale" (L_x) here is one order of magnitude greater than those in relevant studies for small-scale freestream turbulence (Table 1) (e.g. Amandolèse and Széchényi, 2004; Wang et al., 2012; Kim and Xie, 2016; Yu et al., 2017; Algozino et al., 2018; Huang et al., 2020). Synthetic isotropic turbulence was generated at the inflow plane (Fig. 2).

Table 3: Turbulence parameters adopted for the current study. L_x, L_y and L_z denote integral length scales in the streamwise, cross-flow and spanwise directions, respectively. TI denotes turbulence intensity.

Category	L_x	L_y	L_z	TI
Smooth inflow	-	-	-	0%
Large scale 1	$1c$	$0.5c$	$0.5c$	11%
Large scale 2	$1.5c$	$0.75c$	$0.75c$	11%

3.2. Validation

Figures 3 shows a comparison of the aerodynamic coefficients in smooth inflows between the present large-eddy simulations (LES) and reference LES (Huang et al., 2020; Kim and Xie, 2016), and experimental (Lee and Gerontakos, 2004) data at $k_{\text{red}} = 0.05$. The lift coefficient C_L from the present study (Fig. 3 (a)) agrees very well with the reference LES predictions (Huang et al., 2020), and with the wind tunnel measurements (Lee and Gerontakos, 2004). The first peak of the lift predicted by the current LES, which is owing to shedding of the first leading-edge vortex (LEVs) near the maximum angle of attack in the early stage of the dynamic stall, occurs at the same angle of attack as the wind tunnel measurements (Lee and Gerontakos, 2004). The drag coefficient C_D from the current study (Fig. 3 (b)) shows good agreement with those from the reference LES (Kim and Xie, 2016) and experiments (Lee and Gerontakos, 2004).

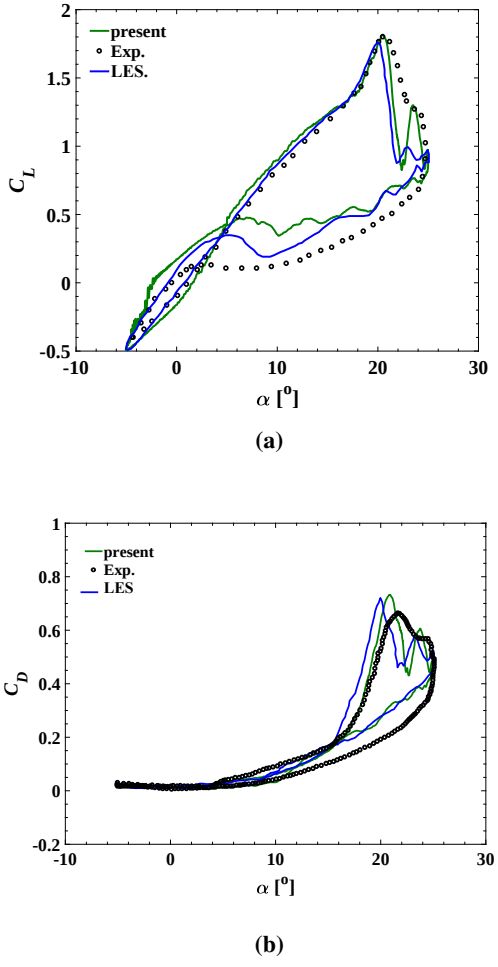

Fig. 3: Aerodynamic coefficient against angle of attack. (a) lift, (b) drag, $k_{\text{red}} = 0.05$. Exp. (Lee and Gerontakos, 2004), LES C_L (Huang et al., 2020), LES C_D (Kim and Xie, 2016).

Figure 4 shows a comparison of aerodynamic coefficients between the present LES and the reference LES (Huang et al., 2020), and experiments (Lee and Gerontakos, 2004) at $k_{\text{red}} = 0.1$. Overall, the present LES data agree very well with the reference LES predictions. The discrepancy between the LES data

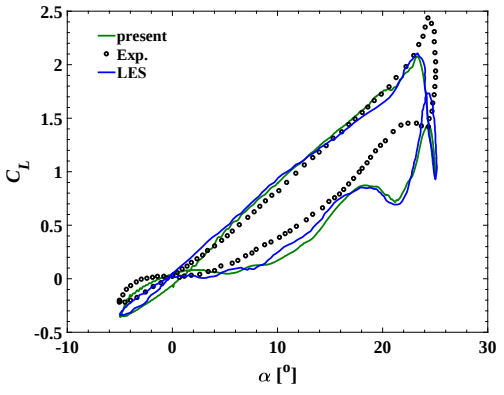

(a)

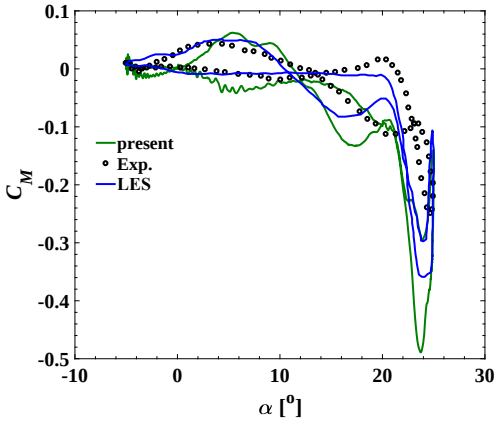

(b)

Fig. 4: Aerodynamic coefficients (a) lift, (b) moment, $k_{\text{red}} = 0.1$. Exp. (Lee and Gerontakos, 2004), LES (Huang et al., 2020).

and the the wind tunnel measurements is likely owing to the technical difficulty for measuring surface pressure at $k_{\text{red}} = 0.1$ (see Kim and Xie (2016)). It is to be noted that the moment is based on the pitching pivot at $0.25c$ from the LE, where is usually the force centre. This means that the moment coefficient is usually very small and extremely sensitive to any small variation of the distribution of surface pressure, which challenges any quantitative comparison. Figure 4b shows that at the stall angle $\alpha = 23°$, the C_M suddenly drops to the lowest peak, and immediately recovers to a small absolute value due to an LEV having grown to mature and shed. This yields a large oscillating torsional force on the wind turbine blade.

4. Impact of large-scale freestream turbulence

4.1. Verification for the synthetic freestream turbulence

A rigorous comparison of auto-correlations at $x/c = -3.5$ and at the inflow plane $x/c = -7$ showed a very small change of integral length scales. The turbulent intensity calculated at $x/c = -3.5$ was approximately $TI = 9\%$ in the core region of the domain (e.g. $1 \leq z/c \leq 2$), while at the inflow plane it was prescribed $TI = 11\%$. The visible difference of the turbulent intensity was due to the exponential decay of freestream turbulence. Therefore, the effective turbulent intensity at $x/c = -3.5$ is the more appropriate quantity if freestream turbulence effect is of concern. The reduced frequencies $k_{\text{red}} = 0.1$

and 0.2 were investigated because they are among the typical frequencies of the wind turbine blade in operation (Leishman, 2002; Gharali et al., 2018).

4.2. Effect on aerodynamic characteristics for k_{red} = 0.1

The effect of large-scale inflow turbulence on aerodynamic characteristics, instantaneous vorticity field, pressure and skin-friction coefficients at different angles of attack for k_{red} = 0.1 is presented and discussed.

4.2.1. Phase-averaged aerodynamic coefficients

Figure 5 shows the effect of incoming large-scales turbulence on aerodynamic characteristics for k_{red} = 0.1. The angles of attack α where the maximum lift, drag and minimum moment occur evidently differ from those of the smooth inflow case, respectively. The magnitudes of the maximum lift, drag and moment coefficients are reduced noticeably in the freestream turbulent flows. These effects are primarily due to the large integral length-scale, in contrast to the effect of small integral length-scale with the same turbulence intensity (Kim and Xie, 2016).

The decrement of the peak lift coefficient for the two freestream large-scale turbulence cases is approximately 20%. In addition, the lift coefficient of the two freestream turbulence cases is reduced by an average of 22% within $15°\downarrow \leq \alpha \leq 22°\downarrow$. The reason for the lift reduction at the pre-stall and during the early stage downstroke is owing to the impingement of the incoming large-scale turbulence on the LEVs and the subsequent discorded LEVs (see Daniels and Xie (2022)). One mechanism is the freestream large-scale turbulence entrainment - the process in which mass is transferred from the external flow regime into the LEV regime (see Fig. 6 (b) - (d) (middle) and (right)). It is to be noted such impingement differs substantially from that due to the small-scale freestream turbulence (e.g. Kim and Xie, 2016; Huang et al., 2020). Studies on small-scale freestream turbulence with integral length-scale not greater than $0.3c$ at the reduced frequency 0.05 (Kim and Xie, 2016) and 0.2 (Huang et al., 2020), showed that the peak lift angle had little change during the upstroke, while the lift had an evident increment during the downstroke.

Another visible effect of large-scale inflow turbulence is the early re-attachment of the boundary layer flow occurs approximately at $\alpha = 11°\downarrow$ for the two large-scale inflow turbulence cases compared to the smooth inflow case, which occurs approximately at $\alpha = 2°\downarrow$ during the downstroke shown in Fig. 5 (a).

The peak drag coefficients for large-scale inflow turbulence cases evidently decreases compared to that of smooth inflow case shown in Fig. 5 (b). The average peak drag coefficient of the large-scale inflow turbulence cases decreased approximately by 21% than that of the smooth inflow case. This evident change of the peak drag coefficient was not observed for the small-scale freestream turbulence case (e.g. Kim and Xie (2016); Huang et al. (2020)). This difference in the peak drag coefficient is well correlated to that in the lift coefficient. It was observed that turbulence does not evidently enhance the drag coefficient.

The impact of the large-scale inflow turbulence on the minimum moment coefficient is similar to those on the lift and drag coefficients. The other visible impact occurs at the dynamic stall angle and during the downstroke shown in Fig. 5 (c). The "memory" (i.e. the area in the hysteresis loop) is reduced evidently for the two large-scale inflow turbulence cases at the high angle of attack and during the downstroke, where separated flows are dominant (see Fig. 6 (e) (middle) and (right)). Again this is owing to the impingement of the incoming large-scale turbulence, resulting in less energetic shed LEVs. This further shows the magnitude of impact on the LEV structures.

Overall, the freestream large-scale turbulence evidently changes the force and moment hysteresis at the given conditions. The data shown in Fig. 5 can draw a conclusion that the aerodynamics force coefficients change evidently due to the impingement of large-scale freestream turbulence on the LEVs.

4.2.2. Vorticity field

Figure 6 shows snapshots of the instantaneous spanwise component of vorticity ω_z at the mid-span plane at $k_{\text{red}} = 0.1$ for the smooth inflow (left), large-scale inflow turbulence cases $L_x = 1c$ (middle) and $L_x = 1.5c$ (right). In the smooth inflow case during $\alpha = 15.8°\uparrow$ to $21.8°\uparrow$ (Fig. 6 (a) - (b) (left)), the boundary layer on the suction side of the blade is largely attached, and a continuous growth of the first LEV is observed near the leading edge. For the two large-scales inflow turbulence cases (Fig. 6 (a) - (b) (middle) and (right)), boundary layer separations are visible, while the first LEVs are difficult to discern due to their interaction with the large-scale inflow turbulence.

In Fig. 6 (c) (left), the first LEV has grown to maturity ready to be detached, resulting in a significant increment of the peak lift coefficient near the dynamic stall angle $\alpha \approx 23.3°\uparrow$. This is consistent with Fig. 5 (a). Such a phenomenon at this phase angle is not evident in the two large-scales inflow turbulence cases (Fig. 6 (c) (middle) and (right)). This is because the incoming large-scale turbulence breaks down and disorders the LEVs structures, which causes the early stall and significant changes in the aerodynamic force coefficients. This is again consistent with Figs. 5 (a) - (c). In addition, the pressure and skin-friction coefficients in Fig. 7 (b) - (d) show further evidence of the LEVs suppression in the two large-scale inflow turbulence cases.

At $\alpha \approx 24.9°\uparrow$ near to the maximum angle of attack (Fig. 6 (d) (left)), the interaction between the first LEV and first TEV is observed for smooth inflow case, which makes the lift recover slightly. However, there is no evidence of two counter-rotating vortices interaction in the two large-scale inflow turbulence cases (Fig. 6 (d) (middle) and (right)), resulting in the sharp drop of lift coefficient(see Figs. 5 (a)).

At $\alpha = 18.8°\downarrow$ for the smooth inflow (Fig. 6 (e) (left)), the third LEV (second LEV not show here) begins to form near the leading edge, resulting in a slight increase in the lift. However, for the two large-scale inflow turbulence cases (Fig. 6 (e) (middle) and (right)), the third LEVs appears very small near the leading edge, and a complete separation of the boundary layer flow is evident, mixing with the incoming large-scale turbulence. This causes a large drop in lift coefficient within the region $15° \downarrow \leq \alpha \leq 22° \downarrow$ (see Fig. 5 (a)).

4.2.3. Blade surface pressure and skin-friction coefficients

The interaction of the large-scale inflow turbulence and the large airfoil-generated eddies (e.g. LEVs) results in break-down, disorder and suppression during the upstroke, and disturbs the separated flows at most phase angles during the downstroke. To get a further understanding of the freestream turbulence impingement on the LEVs, the surface pressure and skin-friction coefficients distributions around the pitching blade were analysed.

Figure 7 shows the spanwise averaged surface pressure and skin friction coefficients (i.e. over $0.75 \leq z/c \leq 2.25$) for the smooth inflow and the two large-scale inflow turbulence cases at the same angles of attack as those in Fig. 6. The C_p (top) and C_f (bottom) in Figure 7(a) show the evident emerging LEV at $x/c \approx 0.05$. Nevertheless, the data from the inflow turbulence case $L_x = 1.5c$ suggests a substantial surface pressure variation results from the impact of the larger-scale inflow turbulence. This confirms (Haan et al., 1998) that a slight increase in integral length-scale increases surface pressure variance on a square prism. It should be noted that the difference between the two large-scales inflow turbulence cases (Fig. 7 (a)) is simply due to the unsteadiness-caused uncertainties as the C_p and C_f were not phase averaged.

It is expected that the LEVs would grow and convect downstream the chord length as the pitching angle increases. Figure 7 (b) shows that the centre of the LEV occurs at $x/c \approx 0.5$, with the start at $x/c \approx 0.37$ and the end at $x/c \approx 0.7$ for the smooth inflow C_p (top) and C_f (bottom) at $\alpha = 21.2°\uparrow$. For the two large-scale inflow turbulence cases, the LEV extents from $x/c \approx 0$ to 0.4 at $\alpha = 21.2°\uparrow$. This is consistent with Fig. 6 (b). A similar phenomenon was observed in Fig. 7 (c) - (d), which further confirms the suppression, breakdown and disorder of the LEVs due to the impact of the freestream large-scale turbulence, which is consistent with the instantaneous vorticity contours taken at the mid-span plane shown in Fig. 6 (c) - (d). The LEV average size is estimated to be $0.52c$ in the smooth inflow case, and $0.28c$ in the freestream turbulence cases, suggesting the significant impact of the freestream turbulence.

The decrease of the lift at $\alpha = 18.6°\downarrow$ shown in Fig. 5 (a) for the large-scale inflow turbulence cases is consistent with Cp and C_f plots shown in Fig. 7 (e). In particular, the case $L_x = 1.5c$ at $0.3 \leq x/c \leq 0.95$ shows very small pressure difference between the pressure and suction sides. Moreover, the case $L_x = 1c$ at $\alpha = 18.6°\downarrow$ shows little signature of LEV on the blade surface, which is again consistent with Fig. 6 (e).

4.3. Effect on aerodynamic characteristics for $k_{red} = 0.2$

The effect of large-scale freestream turbulence on aerodynamic characteristics of the airfoil pitching at $k_{red} = 0.2$ was studied.

4.3.1. Phase-averaged aerodynamic coefficients

Figure 8 shows the effect of large-scale freestream turbulence on aerodynamic characteristics of a pitching wind turbine blade at $k_{red} = 0.2$. Overall, the large-scale freestream turbulence does not significantly change the lift hysteresis loop. The angle of the peak lift is almost the same compared to that of the smooth inflow case. The large-scale freestream turbulence does not evidently affects the peak lift coefficient. Lift coefficient decrements are visible during the downstroke.

The drag coefficient decreases by an average of 15% for the freestream turbulence cases compared to the smooth inflow (Fig. 8 (b)), which is of much lesser magnitude compared to $k_{red} = 0.1$ (Section 4.2). The drag coefficient in the pre-stall phase shows no visible difference between the smooth inflow and turbulent inflow cases.

The lift coefficients in the pre-stall and post-stall regimes do not change noticeably for large-scale inflow turbulence cases compared to the smooth inflow case. It was observed that for both $k_{red} = 0.1$ and 0.2 large-scale inflow turbulence does not consistently enhance the lift coefficients during the downstroke, which is opposite to the lift coefficient increment observed for small-scale inflow turbulence effects reported in wind tunnel test (Amandolèse and Széchényi, 2004) and LES studies (Kim and Xie, 2016; Huang et al., 2020). In addition, the reason for a less visible effect on the lift coefficient hysteresis loop compared to that for $k_{red} = 0.1$ could be owing to the fast pitching motion, which breaks down the incoming large-scale eddies to smaller ones. Kim and Xie (2016) estimated that convective velocity of eddies passing over the airfoil was approximately $U_{conv} = U_\infty/4$ in small-scale freestream turbulence (e.g. the integral length $0.1c$), giving a dimensionless pass-through time $U_\infty/(U_{conv})$=4. The dimensionless oscillation periods for k_{red}=0.1 and 0.2 are respectively 31 and 16. Considering the large-scale freestream turbulence, the convective velocity is even smaller. One quarter of the oscillation period for k_{red}= 0.2 is shorter than the eddy pass-through time, resulting in much more dominant role of the oscillation compared to k_{red}= 0.1.

The most evident impact of freestream turbulence at $k_{red} = 0.2$ is on the moment coefficient at the stall angle and during the downstroke. Figure 8 (c) shows a significant increase of the global minimum moment coefficient for the two inflow turbulence cases compared to the smooth inflow case. The peak-to-peak difference in the global minimum moment coefficient between the smooth inflow and turbulent inflow cases at is approximately 56%. A similar impact on the moment coefficient was observed for $k_{red} = 0.1$ (Fig. 5 (c)). Given that large-scale freestream turbulence has a considerable impact on the aerodynamic force centre location of the pitching blade, one can concluded that the global minimum moment coefficient is strongly dependent on the freestream turbulent quantities.

Overall, the high frequency-pitching motion of the blade ($k_{red} = 0.2$) mitigates the impact of large-scale freestream turbulence on the aerodynamics. An extensive analysis of the vorticity contours, surface pressure and skin-friction coefficients confirms this. In the following sections, only data for $k_{red} = 0.1$ are discussed.

4.4. Dispersive shear stress in the wake

To understand the direct contribution of the pitching motion to the total momentum transfer in the wake region, the term “dispersive stress”, which is widely used for urban and forest environments to

identify the global momentum exchange in the vertical direction due to the local surface changes and the resulted in variations of local time-mean velocities. The dispersive stress is derived based on a "triple" decomposition,

$$u_{i(t)} = \langle \tilde{u}_i \rangle + \hat{u}_i + u'_{i(t)}, \tag{8}$$

where $u_{i(t)}$ is the instantaneous time velocity (i = u,v,w), $\langle \tilde{u}_i \rangle$ is the average of the entire cycle of the phase average velocity (Eq.9), $\hat{u}_i$ is the phase fluctuation of the phase averaged velocity (Eq. 10), $\tilde{u}_i$ is the phase averaged velocity, and $u'_{i(t)}$ is the LES resolved instantaneous turbulent fluctuations (Eq. 11).

$$\langle \tilde{u}_i \rangle = \frac{1}{2\pi} \int_0^{2\pi} \tilde{u}(\Psi) d\Psi \tag{9}$$

$$\hat{u}_i = \tilde{u}_i - \langle \tilde{u}_i \rangle \tag{10}$$

$$u'_{i(t)} = u_{i(t)} - \tilde{u}_i \tag{11}$$

The productions of phase fluctuations $\hat{u}\hat{u}$ and $\hat{u}\hat{v}$ are respectively the dispersive normal stress and dispersive shear stress at the phase angle Ψ. $\langle \hat{u}\hat{u} \rangle$ and $\langle \hat{u}\hat{v} \rangle$ are respectively the averaged dispersive normal stress and dispersive shear stress over the entire cycle. $\widetilde{u'u'}$ and $\widetilde{u'v'}$ are respectively the phase-averaged turbulent normal stress and turbulent shear stress at phase angle Ψ.

The post-processing of the phase stresses data presented in this section was obtained from time series of 75,000 time-steps (3 cycles) each at five wake probes, of which the coordinates were x/c = 2, y/c = 0, and z/c = 1, 1.25, 1.5 1.75 and 2, respectively. At x/c = -3.5, y/c = 0, and z/c = 1.25, 1.5 and 1.75, time series of 50,000 time-steps were sampled each at the three upstream probes.

Considering the homogeneity in the spanwise direction in the sampled region, 6 and 15 cycles of $u_{i(t)}$ were phase averaged to obtain the final phase-averaged velocity $\tilde{u}_i$ for the upstream and the wake probes, respectively.

Figures 9 shows comparison of the phase averaged velocity $\tilde{u}_i$ at the upstream location (x/c = -3.5, y/c = 0) and the wake location (x/c = 2, y/c = 0) , for the two cases $L_x = 1c$ (top) and $L_x = 1.5c$ (bottom). The streamwise phase averaged velocity $\tilde{u}$ oscillates at the upstream probes (x/c = -3.5, y/c =0), because the pitching period is several times the integral time scale of the freestream turbulence, and the averaging is only effectively 6 pitching periods. At the wake probe x/c = 2, the streamwise phase averaged velocity $\tilde{u}$ is dominated by the slow blade pitching motion, with some high-frequency fluctuations. The velocity deficit in the wake is evident at most phase angles, with a maximum just after the maximum angle of attack at $\Psi = 90°$. A similar trend is observed in the two cases $L_x = 1c$ and $L_x = 1.5c$.

The cross-flow phase averaged velocity $\tilde{v}$ and spanwise phase averaged velocity $\tilde{w}$ are very small at at the upstream probes for the two cases (Fig. 9 (a) and (c)). A correlation is visible between $\tilde{u}$, $\tilde{v}$, and $\tilde{w}$. This is again due to the short phase-average at the upstream probes. The cross-flow velocity $\tilde{v}$ at the wake station is very sensitive to the vortex shedding, e.g. at $\Psi \approx 90°$when the first LEV and first TEV detach and shed into the wake (see Fig. 6(c) (left)), and causes strong oscillation of $\tilde{v}$ at this phase angle.

Figure 10 shows the dispersive shear stress $\hat{u}\hat{v}$, turbulent shear stress $\widetilde{u'v'}$ and turbulent kinetic energy $\widetilde{TKE}$ in the wake at x/c = 2 for the two cases $L_x = 1c$ and $L_x = 1.5c$.

The dispersive shear stress $\hat{u}\hat{v}$, turbulent shear stress $\widetilde{u'v'}$, and $\widetilde{TKE}$ show a very small magnitude at lower phase angles (i.e. $-90° \uparrow \leq \Psi < 90° \uparrow$, during the upstroke), whereas at high phase angles (i.e. $90° \uparrow \leq \Psi \leq 270° \downarrow$, during the downstroke) they show a significant change in magnitude. The $\widetilde{TKE}$ values are evidently larger at high phase angles compared to low phase angles. This is attributed to the pitching downstroke motion of the blade, resulting in dominant separated flows in the boundary layer and the shed vortices.

Figure 10 shows that the dispersive shear stress $\hat{u}\hat{v}$ and turbulent shear stress $\widetilde{u'v'}$ in the wake in Fig. 10 (a) and (b) are in the same order of magnitude, but usually with opposite sign at high phase angles ($90° \uparrow \leq \Psi \leq 270° \downarrow$). This suggests that the dispersive shear stress frequently cancel out partially or entirely the turbulent shear stress in the wake, resulting in less resistance to the boundary layer flow on suction side and enhanced lift.

Table 4 shows the dimensionless cycle-averaged total dispersive shear stress $\langle\hat{u}\hat{v}\rangle$, the dimensionless cycle-averaged total turbulent shear stress $\langle\widetilde{u'v'}\rangle$, and the dimensionless total shear stress (τ_a), which is the cycle-averaged sum of the dispersive shear stress and turbulent shear stress. The total dispersive stress for the larger integral length scale case ($L_x = 1.5c$) is nearly half of that for the smaller integral length scale case ($L_x = 1c$), suggesting freestream turbulence with a large integral length scale mitigates the pitching motion effect. The magnitude of the total turbulent stress for the case $L_x = 1.5c$ is slightly greater than that for the ($L_x = 1c$) case, which might be owing to the less dissipation for the former. The dimensionless total shear stresses (τ_a/U_∞^2) for cases $L_x = 1c$ and $L_x = 1.5c$ are respectively -0.0037 and -0.0059.

Table 4: Cycle-averaged dispersive stress $\langle\hat{u}\hat{v}\rangle$, turbulent shear stress $\langle\widetilde{u'v'}\rangle$, and total shear stress ($\tau_a = \langle\hat{u}\hat{v}\rangle + \langle\widetilde{u'v'}\rangle$ at probes ($x/c = 2$, $y/c = 0$) for freestream turbulence cases.

Cases	$\langle\widetilde{u'v'}\rangle/U_\infty^2$	$\langle\hat{u}\hat{v}\rangle/U_\infty^2$	Total shear stress (τ_a/U_∞^2)
$L_x = 1c$	-0.0079	0.0042	-0.0037
$L_x = 1.5c$	-0.0083	0.0023	-0.0059

The large magnitude of the total dispersive stress in the wake region, suggesting the significant role of the large-scale and slow unsteady flow. It is to be noted that such is more a two-dimensional large-scale flow that has little dissipation and can convert to an extremely long distance in the wake.

4.5. Quadrant analysis

To understand more of the dispersive and turbulent shear stresses in the wake region, the widely used quadrant analysis (Wallace et al., 1972) is used. The quadrant analysis is a useful tool to determine more insight into the fractional contribution of each of the four categories of turbulent shear stress, as well as the dispersive stress. The four categories are: Q1 $(+u', +v')$, Q2 $(-u', +v')$, Q3 $(-u', -v')$ and Q4 $(+u', -u')$, which are called quadrants of the Reynolds stress plane (Wallace et al., 1972; Wallace, 2016). The quadrant analysis for the dispersive stress is the same as for the turbulent stress, except for using the phase fluctuations $\hat{u}_i$ instead of the turbulent fluctuations u_i'. The Q2 and Q4 relate to gradient-type motion, which is the ejection and sweep quadrants, and they make the largest contributions to the turbulent shear stress, while Q1 and Q3 relate to counter gradient-type motion, which is the outward and inward interactions quadrants. Using the same time series as in Sect.4.4, this quadrant analysis technique is used for the dispersive shear stress $\hat{u}\hat{v}$ and turbulent shear stress $u'v'$ in the wake.

Figure 11 (a) and (b) shows the quadrants of the turbulent shear stress $u'v'$ for the two cases $L_x = 1c$ and $L_x = 1.5c$, respectively. The quadrants Q2 and Q4 of the turbulent shear stress for the two cases are evidently dominant compared to Q1 and Q3 (Fig. 11 (a)). This means that the ejection and sweep events are the largest contributors to the turbulent shear stress in the wake flows, same as those in steady turbulent boundary layer flow. Nevertheless, the ejection events are slightly stronger than the sweep events.

On the contrary, Figure 12 show that the quadrants Q1 and Q3 for the dispersive shear stress $\hat{u}\hat{v}$ are dominant compared to the quadrants Q2 and Q4. This means that the outward and inward events

contributes most to the dispersive shear stress in the wake of a pitching wind turbine blade, opposite to the turbulent shear stress (Fig.11).

The cycle-averaged dispersive shear stresses $\langle \hat{u}\hat{v} \rangle$ are estimated being 0.0042 and 0.0023 for the cases $L_x = 1c$ and $L_x = 1.5c$ respectively. The positive dispersive shear stresses suggests a cancel out to the turbulent shear stress in the wake, resulting in an effective propulsion to the boundary layer flow in the suction side of the blade, and an enhancement of the lift. Overall, the pitching motion at k_{red}=0.1 significantly reduces the magnitude of the total shear stress in the wake. The freestream turbulence with the integral length scales much greater than the chord length mitigates this effect.

5. Discussions and concluding remarks

The paper reports the LES study on impact of large-scale freestream turbulence (FST), with the streamwise integral length scale (L_x) ranging from $1c$ - $1.5c$ and the turbulent intensity TI = 11%, on the aerodynamic characteristics of a pitching wind turbine blade section for reduced frequencies k_{red} = 0.1 and 0.2. Vigorous validation and verification were carried out.

The impact of large-scale freestream turbulence of streamwise integral length-scale, $L_x \geq 1c$ and TI = 11% is evident on the lift, drag and moment coefficients of the pitching wind turbine blade at the reduced frequency k_{red} =0.1, of which the pitching period is about seven times greater than the eddy convection time over the airfoil. The magnitude of the lift and drag, in particular the peak values, are evidently reduced by the large-scale freestream turbulence. These are attributed to the early separation of the boundary layer during the upstroke, and the disordered, broken-down, and slow convected leading-edge vertices (LEVs), which suffer from the impingement of the incoming large-scale turbulence. This is consistent with the argument that large-scale freestream turbulence reduces the aerodynamics performance of static aerofoils (Wang and Xiao, 2021; Herbst et al., 2018; Mahmoodilari, 2012). It is to be noted that the small-scale freestream turbulence (e.g. $L_x/c \leq 0.1$) (Huang et al. (2020); Kim and Xie (2016)) increases the lift during the downstroke and the aerodynamics performance. This suggests the crucial role of the integral length scales in studying the freestream turbulence effect.

At a higher pitching frequency (i.e. k_{red} = 0.2), of which the pitching period is about three times the eddy convection time over the airfoil, the effect of large-scale freestream turbulence on the lift coefficients is evidently mitigated, compared to a lower reduced frequency k_{red} = 0.1. This is because the time scale of the dominant periodic pitching motion is close to that of the incoming turbulence, resulting in an weakened impact of the freestream turbulence.

The pitching motion of the wind turbine contributes significantly to the total shear stress in the wake. The cycle-averaged dispersive shear stress in the wake is in the same magnitude but with an opposite sign, compared to the cycle-averaged turbulent shear stress. This has two crucial implications. 1) the dispersive shear stress frequently cancels out partially or entirely the turbulent shear stress in the wake, resulting in less resistance to the boundary layer flow on suction side and enhanced lift. 2) the large-scale and slow unsteady flow in the wake plays a crucial role on the extremely long-distance convection in the wake, as such more two-dimensional large-scale flow has weak dissipation.

The cycle-averaged dispersive stress in freestream turbulent flow with the integral length scale $L_x = 1.5c$ is nearly half of that with the integral length scale $L_x = c$, suggesting that incoming turbulent eddies much greater than the chord length yield a reduced impact. This confirms the early observations that freestream turbulence with the integral length one order of magnitude greater than the chord length has little effect. In summary for the considered Reynolds number, FST with integral length scales close to or greater than the chord length can evidently reduce the lift coefficient, whereas FST with integral length scales much less than the chord length increases the lift coefficient, in particular during the downstroke of a pitching airfoil (e.g. Kim and Xie, 2016). The FST effect can be largely mitigated when the pitching period is close to the eddy convection time over the airfoil.

Acknowledgement. The authors are grateful to the United Kingdom Turbulence Consortium (UKTC) computational resources support under grant EPSRC, for access to ARCHER high-performance computational resources. TEB appreciate the provision of the IRIDIS4 computational resources at the University of Southampton.

Funding Statement. ZTX is grateful for the EPSRC support (EP/M022692/1) on this study. TEB is grateful for the funding support by the Petroleum Technology Development Fund (PTDF) Nigeria (PTDF/1052/17/PHD/028).

Declaration of Interests. The authors declare no conflict of interest.

Data Availability Statement. The datasets generated during and/or analysed during the current study are available from the corresponding author on reasonable request.

Ethical Standards. The research meets all ethical guidelines, including adherence to the legal requirements of the study country.

References

M. L. Aitken, B. Kosović, J. D. Mirocha, and J. K. Lundquist. Large eddy simulation of wind turbine wake dynamics in the stable boundary layer using the weather research and forecasting model. *Journal of Renewable and Sustainable Energy*, 6(3): 033137, 2014.

S. Algozino, J. Marañón Di Leo, J. S. Delnero, and G. Capittini. Turbulence effect on flat plate pitching airfoil. *2018 Fluid Dyn. Conf.*, pages 1–11, 2018.

X. Amandolèse and E. Széchényi. Experimental study of the effect of turbulence on a section model blade oscillating in stall. *Wind Energy*, 7(4):267–282, 2004. ISSN 10954244.

C. E. Badoe, Z.-T. Xie, and N. D. Sandham. Large eddy simulation of a heaving wing on the cusp of transition to turbulence. *Computers & Fluids*, 184:64–77, 2019.

L. Bowen, A. Celik, and M. Azarpeyvand. A thorough experimental investigation on aerofoil turbulence interaction noise. *Physics of Fluids*, 2023.

T. E. Boye. *Aerodynamics of a pitching wind turbine blade and the large-scale turbulence impact*. PhD thesis, University of Southampton, 2022.

T. E. Boye and Z.-T. Xie. Aerodynamics of a pitching wind turbine blade at high reduced frequencies. *Journal of Wind Engineering and Industrial Aerodynamics*, 223:104935, 2022.

L. Browne, R. Antonia, and D. Shah. Turbulent energy dissipation in a wake. *Journal of Fluid Mechanics*, 179:307–326, 1987.

L. W. Carr. Dynamic stall progress in analysis and prediction. *J. Aircr.*, 25(1):6–17, 1985. ISSN 0021-8669.

N. Chiereghin, D. Cleaver, and I. Gursul. Unsteady measurements for a periodically plunging airfoil. In *55th AIAA Aerospace Sciences Meeting*, page 0996, 2017.

S. J. Daniels and Z.-T. Xie. An overview of large-eddy simulation for wind loading on slender structures. *Proceedings of the Institution of Civil Engineers-Engineering and Computational Mechanics*, pages 1–67, 2022.

A. Gandhi, B. Merrill, and Y. Peet. Effect of reduced frequency on dynamic stall of a pitching airfoil in a turbulent wake. *AIAA SciTech Forum - 55th AIAA Aerosp. Sci. Meet.*, pages 1–15, 2017.

K. Gharali, E. Gharaei, M. Soltani, and K. Raahemifar. Reduced frequency effects on combined oscillations, angle of attack and free stream oscillations, for a wind turbine blade element. *Renew. Energy*, 115:252–259, 2018. ISSN 18790682.

C. J. Greenshields. OpenFOAM user guide version 5. Technical report, 2017.

F. L. Haan, A. Kareem, and A. Szewczyk. The effects of turbulence on the pressure distribution around a rectangular prism. *J. Wind Eng. Ind. Aerodyn.*, 77-78:381–392, 1998. ISSN 01676105.

M. M. Hand. *Mitigation of wind turbine/vortex interaction using disturbance accommodating control*. University of Colorado at Boulder, 2004.

S. L. Herbst, C. J. Kähler, and R. Hain. Influence of large-scale free-stream turbulence on an SD7003 airfoil at low reynolds numbers. *2018 Appl. Aerodyn. Conf.*, 2018.

X. Huang, M. Albers, P. S. Meysonnat, M. Meinke, and W. Schröder. Analysis of the effect of freestream turbulence on dynamic stall of wind turbine blades. *Int. J. Heat Fluid Flow*, 85(August 2019), 2020. ISSN 0142727X.

M. Inagaki, T. Kondoh, and Y. Nagano. A mixed-time-scale SGS model with fixed model-parameters for practical LES. *J. Fluids Eng. Trans. ASME*, 127(1):1–13, 2005. ISSN 00982202.

H. Jasak and Ž. Tuković. Automatic mesh motion for the unstructured Finite Volume Method. *Trans. Famena*, 30(2):1–20, 2006. ISSN 13331124.

H. Jasak, H. G. Weller, and A. D. Gosman. High resolution NVD differencing scheme for arbitrarily unstructured meshes. *Int. J. Numer. Methods Fluids*, 31(2):431–449, 1999. ISSN 02712091.

A. Jimenez, A. Crespo, E. Migoya, and J. Garcia. Advances in large-eddy simulation of a wind turbine wake. *J. Phys. Conf. Ser.*, 75(1):0–13, 2007. ISSN 17426596.

J. C. Kaimal and J. J. Finnigan. *Atmospheric boundary layer flows: their structure and measurement*, volume 32. Oxford University press., 1994. ISBN 9780195062397.

V. R. Kasibhotla and D. Tafti. Dynamic stall simulation of flow over naca0012 airfoil at 1 million reynolds number. In *ASME International Mechanical Engineering Congress and Exposition*, volume 57465, page V07AT09A020. American Society of Mechanical Engineers, 2015.

Y. Kim. *Wind Turbine Aerodynamics in Freestream Turbulence*. PhD thesis, University of Southampton, 2013.

Y. Kim and Z. T. Xie. Modelling the effect of freestream turbulence on dynamic stall of wind turbine blades. *Comput. Fluids*, 129:53–66, 2016. ISSN 00457930.

Y. Kim, I. Castro, and Z. Xie. Divergence-free turbulence inflow conditions for large-eddy simulations with incompressible flow solvers. *Comput. Fluids*, 84:56–68, 2013. ISSN 00457930.

L. Krishnan, N. D. Sandham, and J. Steelant. Shock-wave/boundary-layer interactions in a model scramjet intake. *AIAA J.*, 47 (7):1680–1691, 2009. ISSN 00011452.

A. S. Lau, S. Haeri, and J. W. Kim. The effect of wavy leading edges on aerofoil–gust interaction noise. *Journal of Sound and Vibration*, 332(24):6234–6253, 2013.

T. Lee and P. Gerontakos. Investigation of flow over an oscillating airfoil. *J. Fluid Mech.*, 512:313–341, 2004. ISSN 00221120.

J. G. Leishman. Challenges in modeling the unsteady aerodynamics of wind turbines. In *21st ASME Wind Energy Symp. 40th AIAA Aerosp. Sci. Meet. Reno, NV.*, pages 141–167, 2002.

J. Lundquist and L. Bariteau. Dissipation of turbulence in the wake of a wind turbine. *Boundary-Layer Meteorology*, 154(2): 229–241, 2015.

M. Mahmoodilari. *The Effect of Turbulent Flow on Wind Turbine Loading and Performance*. PhD thesis, University of Manchester, 2012.

V. Maldonado, L. Castillo, A. Thormann, and C. Meneveau. The role of free stream turbulence with large integral scale on the aerodynamic performance of an experimental low Reynolds number S809 wind turbine blade. *J. Wind Eng. Ind. Aerodyn.*, 142:246–257, 2015. ISSN 01676105.

W. J. McCroskey. Unsteady airfoils. *Annual review of fluid mechanics*, 14(1):285–311, 1982.

B. Raverdy, I. Mary, P. Sagaut, and N. Liamis. High-resolution large-eddy simulation of flow around low-pressure turbine blade. *AIAA J.*, 41(3):390–397, 2003. ISSN 00011452.

S. Ravi, S. Watkins, J. Watmuff, K. Massey, P. Peterson, and M. Marino. Influence of Large-Scale Freestream Turbulence on the Performance of a Thin Airfoil. *AIAA J.*, 50(11):2448–2459, 2012. ISSN 0001-1452.

S. Ravi, S. Watkins, J. Watmuff, and A. Fisher. Transient loads occurring over a thin airfoil subjected to large-scale freestream turbulence. *AIAA J.*, 51(6):1473–1485, 2013. ISSN 00011452. http://dx.doi.org/10.2514/1.J052142.

M. S. Shohag, E. C. Hammel, D. O. Olawale, and O. Okoli. Damage mitigation techniques in wind turbine blades: A review. *Wind Engineering*, 41(3):185–210, 2017.

C. Sicot, S. Aubrun, S. Loyer, and P. Devinant. Unsteady characteristics of the static stall of an airfoil subjected to freestream turbulence level up to 16%. *Exp. Fluids*, 41(4):641–648, 2006. ISSN 07234864.

J. Stack. Technical notes national advi sory. (364), 1931.

R. B. Stull. *An introduction to boundary layer meteorology*. Kluwer Academic Publishers, 1988. ISBN 9027727686.

H. Sun, X. Gao, and H. Yang. A review of full-scale wind-field measurements of the wind-turbine wake effect and a measurement of the wake-interaction effect. *Renewable and Sustainable Energy Reviews*, 132:110042, 2020.

J. M. Wallace. Quadrant analysis in turbulence research: history and evolution. *Annual Review of Fluid Mechanics*, 48:131–158, 2016.

J. M. Wallace, H. Eckelmann, and R. S. Brodkey. The wall region in turbulent shear flow. *Journal of Fluid Mechanics*, 54(1): 39–48, 1972.

R. Wang and Z. Xiao. Influence of free-stream turbulence on the aerodynamic performance of a three-dimensional airfoil. *AIP Advances*, 11(7):075304, 2021.

S. Wang, D. B. Ingham, L. Ma, M. Pourkashanian, and Z. Tao. Turbulence modeling of deep dynamic stall at relatively low reynolds number. *Journal of Fluids and Structures*, 33:191–209, 2012.

X. Wu. Inflow Turbulence Generation Methods. *Annu. Rev. Fluid Mech.*, 49(1):23–49, 2017. ISSN 0066-4189.

Z. T. Xie and I. P. Castro. Efficient generation of inflow conditions for large eddy simulation of street-scale flows. *Flow, Turbul. Combust.*, 81(3):449–470, 2008. ISSN 13866184.

Z.-T. Xie and V. Fuka. A note on spatial averaging and shear stresses within urban canopies. *Boundary-layer meteorology*, 167 (1):171–179, 2018.

J. M. Yu, T. S. Leu, and J. J. Miau. Investigation of reduced frequency and freestream turbulence effects on dynamic stall of a pitching airfoil. *J. Vis.*, 20(1):31–44, 2017. ISSN 18758975.

Z. Zhang, Z. Wang, and I. Gursul. Effects of geometry of wings submerged in turbulent bluff-body wake. *AIAA Journal*, 61(1): 241–254, 2023.

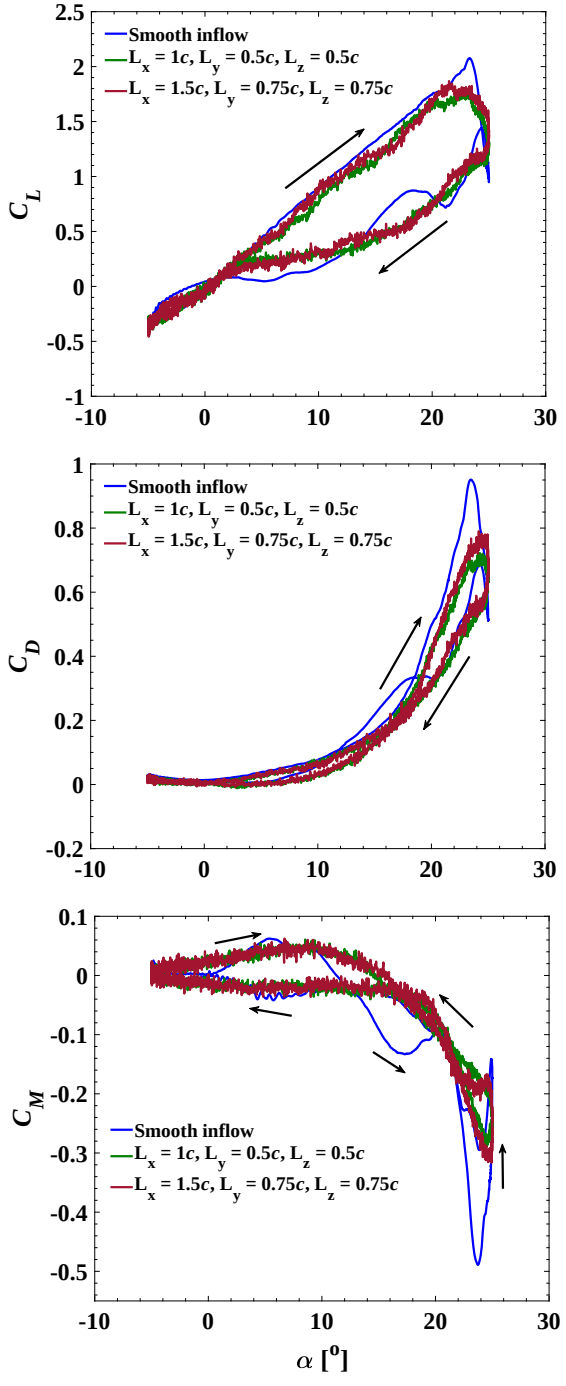

Fig. 5: Effect of large-scale turbulence on aerodynamic coefficients. (a) lift, (b) drag and (c) moment, $k_{\mathrm{red}} = 0.1$.

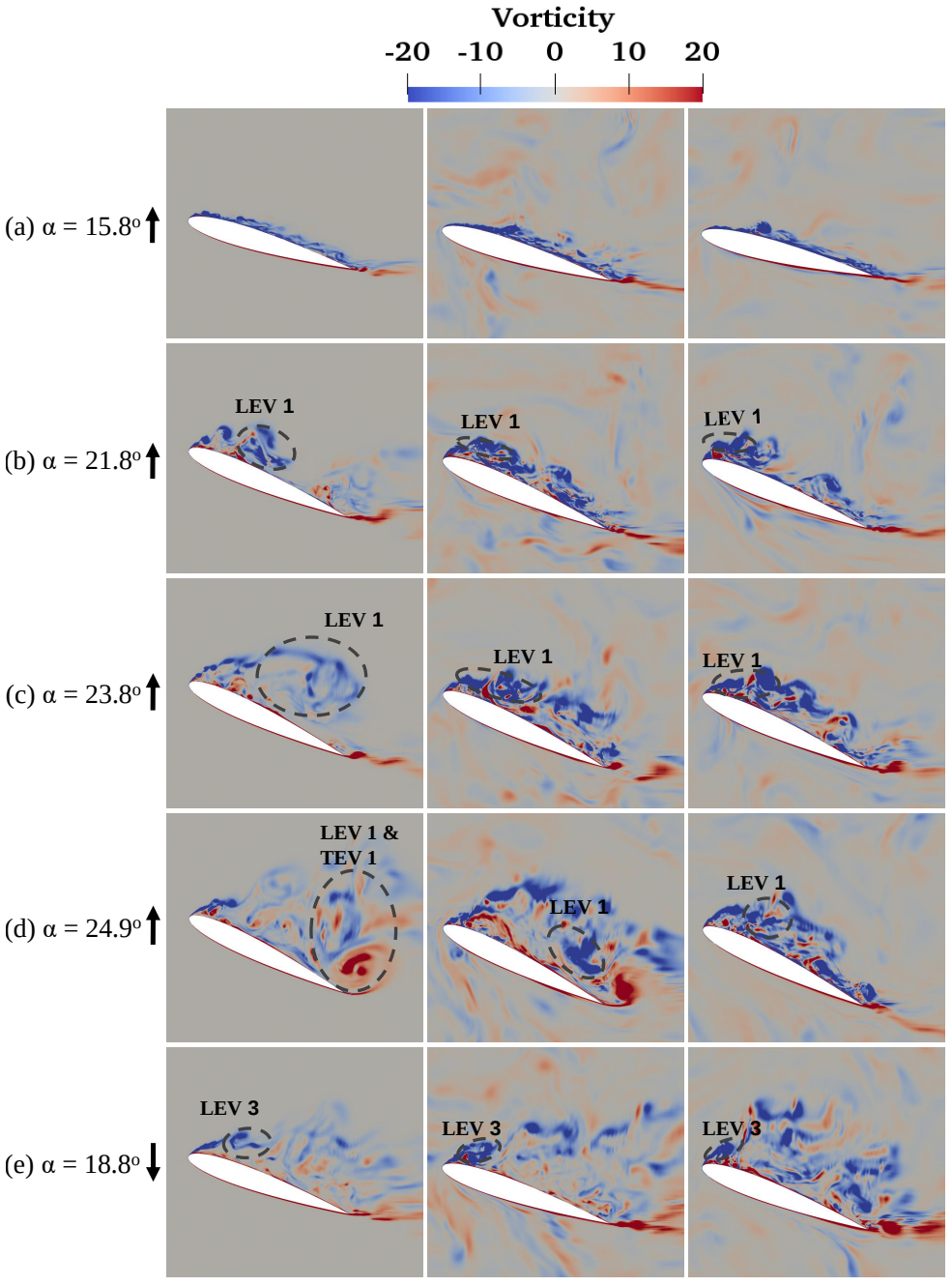

Fig. 6: Snapshots of the instantaneous vorticity ω_z contours normalised by c and U_∞ at $k_{\text{red}} = 0.1$. (left) smooth inflow, (middle) $L_x = 1c$, (right) $L_x = 1.5c$. (a) $\alpha = 15.8°\uparrow$, (b) $\alpha = 21.8°\uparrow$, (c) $\alpha = 23.8°\uparrow$, (d) $\alpha = 24.9°\uparrow$, (e) $\alpha = 18.8°\downarrow$. The dashed ellipse marks the LEV's size and location as suggested in Fig. 7 by using the skin-friction.

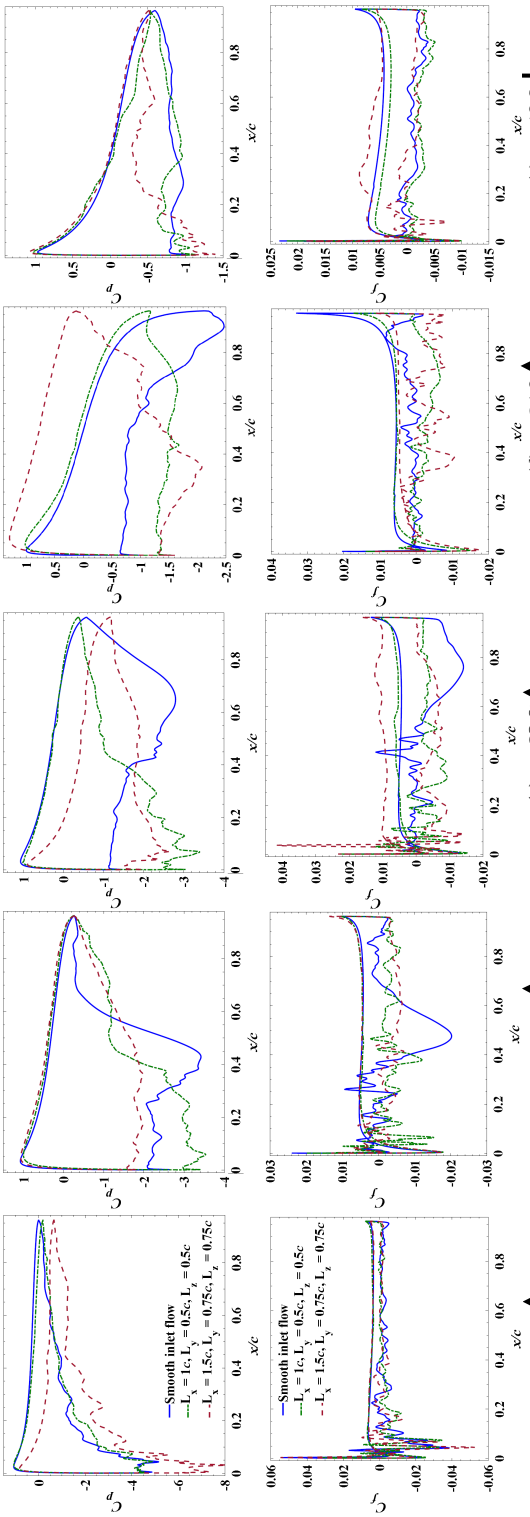

Fig. 7: spanwise-averaged ($0.75 \leq z/c \leq 2.25$) surface forces at $k_{\mathrm{red}} = 0.1$. (top) Pressure coefficient, (bottom) Skin friction coefficient. (a) $\alpha = 15.8°\uparrow$, (b) $\alpha = 21.8°\uparrow$, (c) $\alpha = 23.8°\uparrow$, (d) $\alpha = 24.9°\uparrow$, (e) $\alpha = 18.8°\downarrow$.

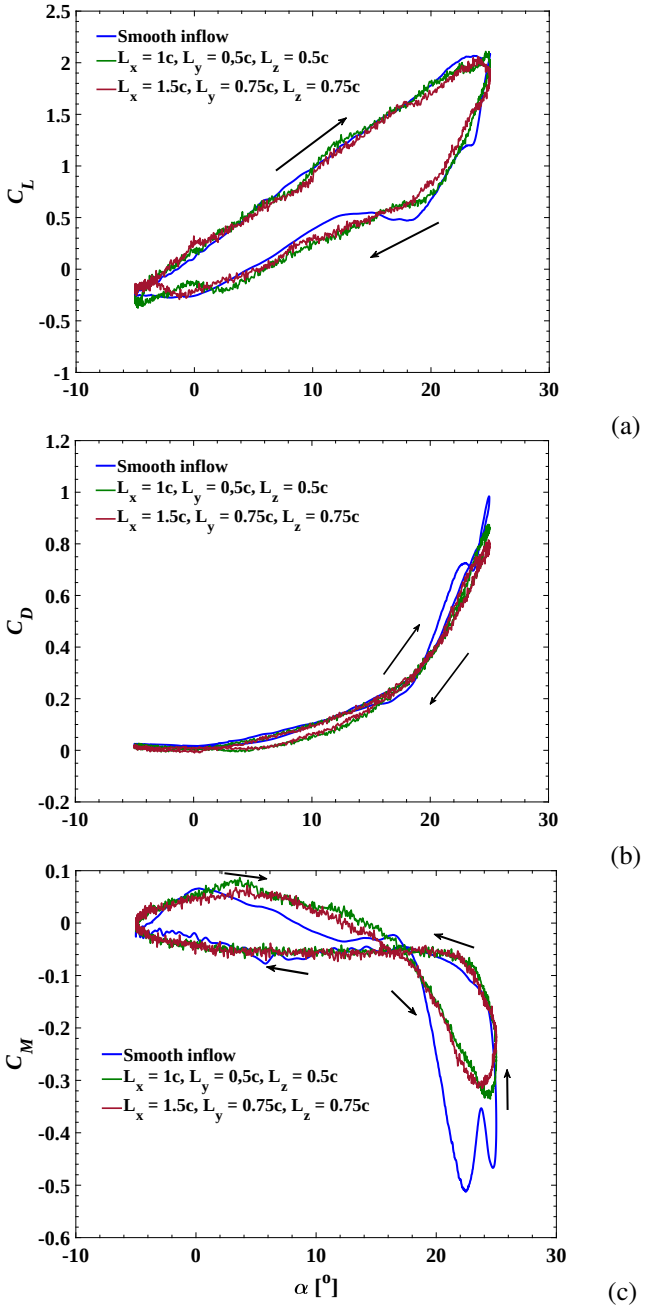

Fig. 8: Effect of large scale turbulence on aerodynamic coefficients. (a) lift, (b) drag, and (c) moment, $k_{\text{red}} = 0.2$.

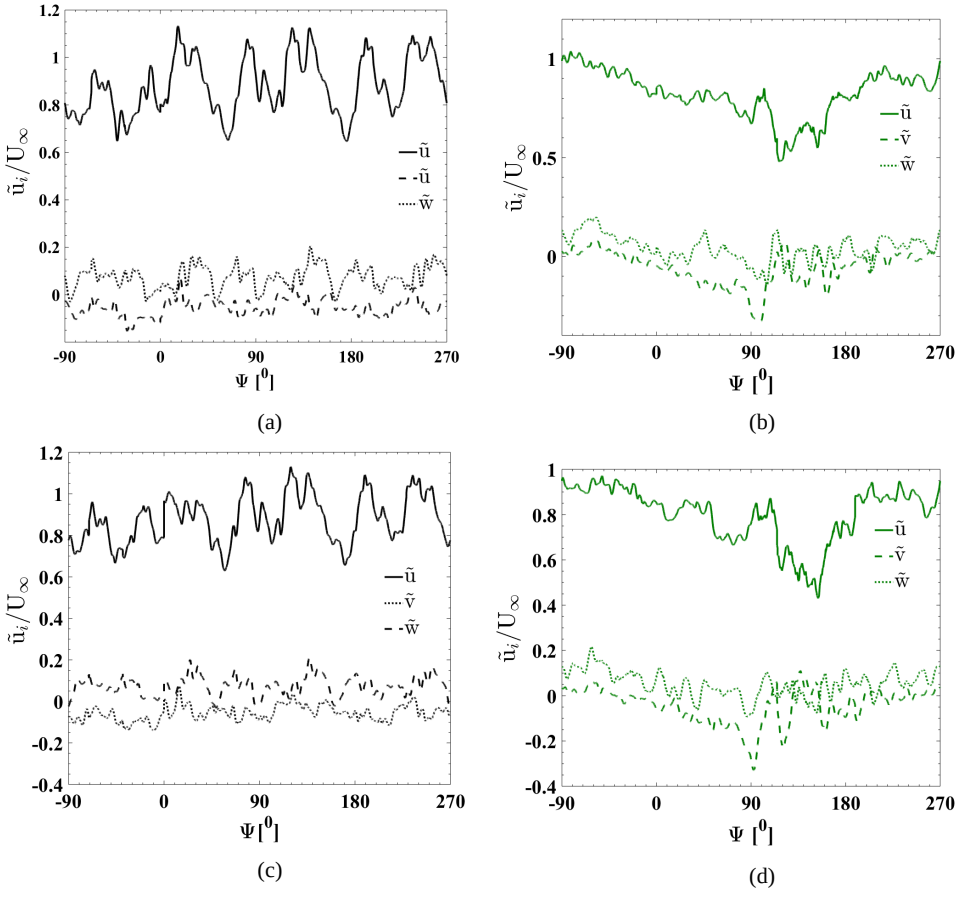

Fig. 9: Phase averaged velocity $\tilde{u}_i/U_\infty$ at k_{red} = 0.1. Case L_x = 1c (top), (a) x/c = -3.5, y/c = 0, (b) x/c = 2, y/c = 0. Case L_x = 1.5c (bottom), (c) x/c = -3.5, y/c = 0, (d) x/c = 2, y/c = 0. See Fig. 1 for the phase angle Ψ and the angle of attack α

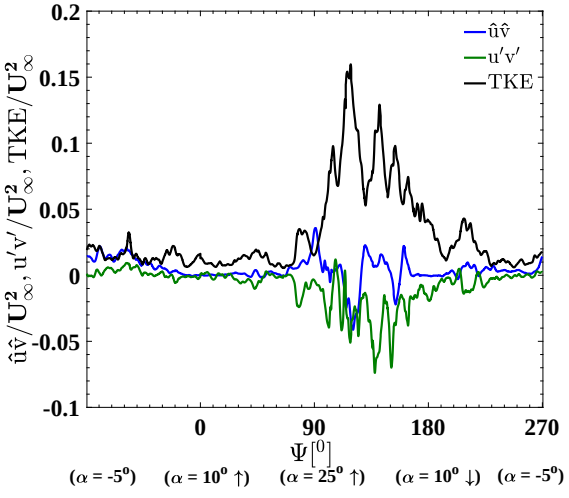

(a)

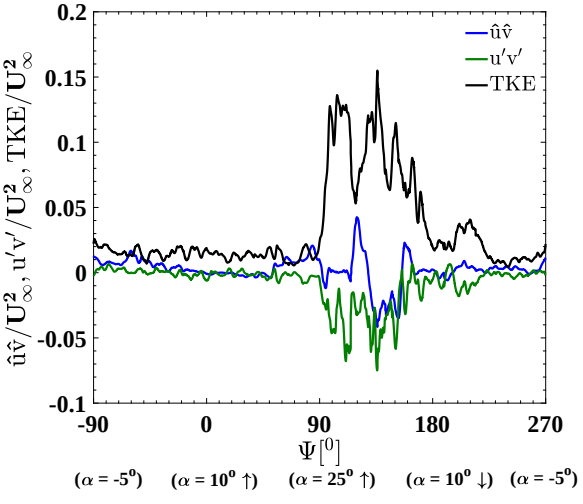

(b)

Fig. 10: Dimensionless dispersive shear stress $\hat{u}\hat{v}$, turbulent shear stress $\widetilde{u'v'}$, and turbulent kinetic energy $\widetilde{TKE}$ at x/c = 2, y/c =0, and k_{red} = 0.1. (a) case $L_x = 1c$, (b) case $L_x = 1.5c$

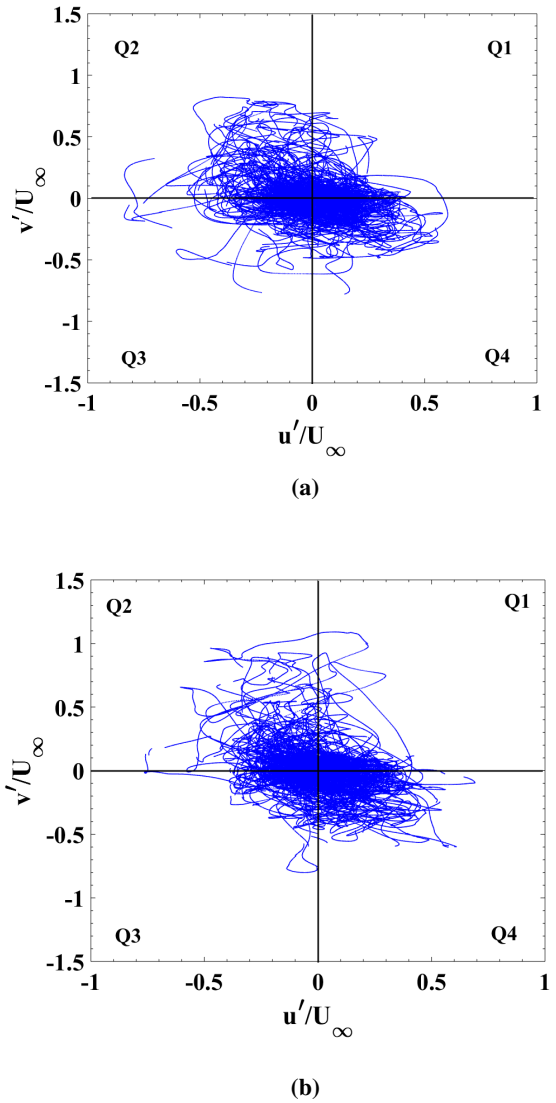

Fig. 11: Quadrant analysis for the dimensionless instantaneous turbulent velocities u′ and v′ at x/c = 2, y/c =0, and k_{red} = 0.1. (a) case $L_x = 1c$, (b) case $L_x = 1.5c$

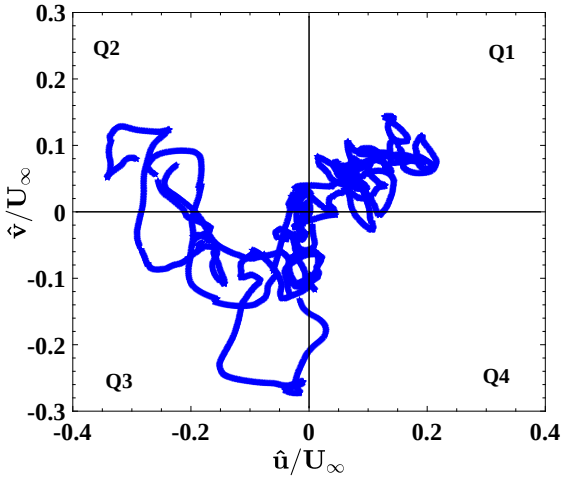

(a)

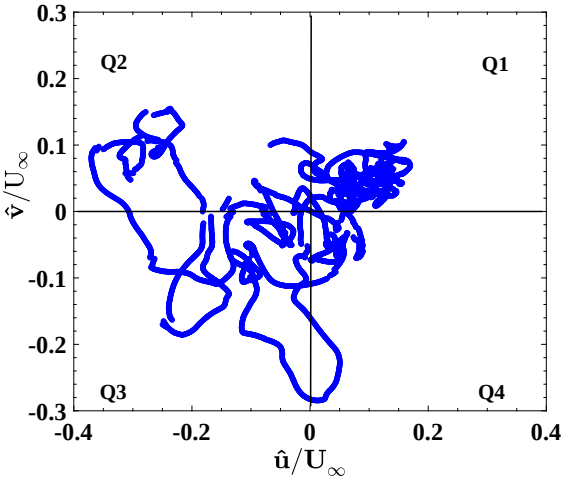

(b)

Fig. 12: Quadrant analysis for the dimensionless phase fluctuations û and v̂ at location x/c = 2, y/c =0, and k_{red} = 0.1. (a) case $L_x = 1c$, (b) case $L_x = 1.5c$